Supporting Information

The joint effect of elasticity, interaction energy and entropy on behavior of pressure- and temperature-induced electronic bi-stability in the family of two-dimensional Hoffman-like coordination polymers

Ruixin Li, [a] Georgiy Levchenko, [*, a, c] Francisco Javier Valverde-Muñoz, [b] Ana Belén Gaspar, [*, b] Victor V. Ivashko, [d] Quanjun Li, [a] Wei Xu, [e] Hennagii Fylymonov, [c] Bingbing Liu, [a] Jose Antonio Real [*, b]

[a] State Key Laboratory of Superhard Materials, International Centre of Future Science, Jilin University, Changchun 130012, China

[b] Institut de Ciència Molecular, Departament de Química Inorgànica, Universitat de València, E-46980 València, Spain;

[c] Donetsk Institute of Physics and Engineering named after A. A. Galkin, Kyiv 03028, Ukraine

[d] Department of Correlation Optics, Chernivtsi National University, Chernivtsi 58012, Ukraine

[e] State Key Laboratory of Inorganic Synthesis and Preparative Chemistry, College of Chemistry, Jilin University, Changchun 130012, China

Corresponding Authors

Georgiy Levchenko: g-levch@ukr.net

Ana Belén Gaspar: ana.b.gaspar@uv.es

Jose Antonio Real: jose.a.real@uv.es

Experimental Procedures

Material synthesis. The microcrystalline powders of compounds $[Fe(Fpz)_2Pd(CN)_4]$ and $[Fe(Fpz)_2Ni(CN)_4]$ were synthesized according to reference S1. [S1]

The magnetic measurement under hydrostatic pressure. The magnetic susceptibility of the microcrystalline powder with temperature is measured on a Quantum Design SQUID magnetometer (SQUID-VSM) with a 7 T magnetic field, and the test is carried out under the conditions of 1 T and 1 K/min. The hydrostatic pressure is provided by a piston-cylinder press made of hard beryllium bronze, and low-viscosity silicone oil (silicone oil DC 200, viscosity: 10, FLUKA) is used as the pressure transmission medium. Its melting point at atmospheric pressure is 220 K. The non-hydrostaticity of pressure is less than 0.025 GPa in all using pressure interval. Cylindrical samples with a diameter of 1.2 mm and a length of 5 ~ 7 mm were made and put into the pressure chamber. The pressure inside the pressure cell is generated by the standard mechanical press and its value installed using oil manometer. Beside that the pressure is measured precisely by the pressure dependence of the superconducting temperature of high-purity lead around temperature 7 K. [S2] The difference of pressure in the two measurements does not exceed 0.025 GPa, which is within the experimental error and is caused by a decrease in pressure with a decrease in temperature. Such a small pressure difference is achieved by the design of the cell and the use of an extremely small amount of silicone oil in it. The hydrostatic pressure is ensured by the low viscosity oil and its high solidification pressure (about 12 GPa). The cell contribution to the useful signal at atmospheric pressure was not observed. The influence of the solidification on the useful signal also was not observed (Figure S1a). But at high pressures, the cell manifests itself and for its subtraction, the assumption is used that the magnetic moment of the sample at room temperature changes under pressure by an amount that can be neglected and the product of $\chi_m T$ does not change when the temperature decreases before the transition begins. Therefore, the measured values of the $\chi_m T$ at room temperature (Figure S1b) are reduced to the magnitude of it at atmospheric pressure. This eliminates the influence of the cell on pressure measurements. Before that the correction of the diamagnetism is performed for ambient pressure measurements using Pascal's constants.

Raman spectrum under hydrostatic pressure. The diamond anvil cell (DAC) consists of a pair of 1A ultra-

low fluorescence diamond anvils with a 500 μm anvil culet. The microcrystal sample is placed in a hole with a diameter of 180 μm drilled on a stainless-steel gasket pre-compressed to a thickness of 50 ~ 60 μm. Silicone oil is used as a pressure transmission medium, and its solidification pressure at room temperature is 12 GPa, so it can provide better hydrostatic properties by staying liquid in the experimental pressure range.[S3] The pressure in the experiment is determined by the pressure dependence of the R1 fluorescence emission of the ruby in the pressure chamber.[S2] The Raman spectra were measured using a Horiba Jobin Yvon HR800 confocal spectrometer. Before detecting the Raman spectra, the spectrometer was calibrated by the standard Raman peak of a silicon wafer at 520.7 cm^{-1}. The Raman signal excited by a 473 nm laser (Laser Power: 1 mW, Objective: 20x) was recorded by a Princeton Instruments CCD detector and collected in the frequency range of 200 ~ 2400 cm^{-1}. The Rayleigh scattering was removed using a holographic notch filter. We have performed temperature-variable Raman experiments prior to the high-pressure experiments, carefully examining the role of thermal effects around the transition temperature, combined with laser intensities previously used by others in SCO's Raman experiments. Thermal effects are negligible during pressure-induced spin transition.

High-pressure infrared spectroscopy. In situ high-pressure infrared spectroscopy is measured in the Bruker spectrometer (VERTEX 80v) in the range of 2000 ~ 400 cm^{-1}. The objective of the microscope is 15x. The sample is placed in a hole with a diameter of 150 μm drilled on a T301 stainless steel gasket pre-compressed to a thickness of 50 ~ 60 μm. In infrared experiments, potassium bromide (KBr) is used as a pressure transmission medium. The potassium bromide (KBr) should be dried before each experiment to avoid the influence of water molecules. At pressures lower than 2 GPa, the non-hydrostatic pressure of KBr is lower than 0.1 GPa, while the structural phase transition occurs at 2 GPa, resulting in a decrease in the hydrostatic properties, and its non-hydrostatic pressure becomes 0.2 GPa.[S4] Ruby particles are placed in the sample chamber for pressure determination in the experiment.

High-pressure UV-Vis absorption spectrum. The absorption spectrum of the sample under hydrostatic pressure was measured using a Shimadzu UV-2101PC spectrophotometer. The sample was made by pre-pressing the microcrystalline powder into a transparent uniform sheet. The sample did not reach nanometer size, so the size effect is not obvious.[S5-S6] And the pressure we applied is relatively small, below the spin transition pressure, combined with Raman, IR and XRD, the compound returns to the initial state after the

pressure is released. Therefore, the properties of the sample do not change. Then it is placed in the hole drilled in the stainless-steel gasket, and silicone oil is used as the pressure transmission medium. The pressure is calibrated by the fluorescence emission of ruby in the sample chamber.

Powder X-ray diffraction under hydrostatic pressure. The experiment was performed on the polycrystalline sample loaded into a diamond anvil cell (DAC). The diameter of the diamond anvil is 600 μm. The stainless-steel gasket is pre-compressed to 50 ~ 60 μm and a hole with a diameter of 300 μm is drilled. Place the sample as much as possible in the sample chamber, and then drop silicone oil as the pressure transmission medium. The pressure is determined by the fluorescence of ruby. High-pressure X-ray diffraction data were obtained using graphite monochromated Mo-K_α radiation (λ = 0.71073 Å) on Rigaku Synergy Custom FR-X Diffractometer equipped with a Hybrid Photon Counting (HPC) X-ray detector (HyPix-6000HE). Data collection and preliminary data reduction were performed with the CrysAlis software package. Rietveld refinements were performed using GSAS software. The atom positions were not refined but fixed according to the phase in ambient conditions. The background was reduced using a manual background combined with a Chebyshev polynomial. The unit-cell parameters as well as scale factors were refined. Finally, the profile was fitted using a Thompson-Cox-Hastings pseudo-Voigt equation.

Results and Discussion

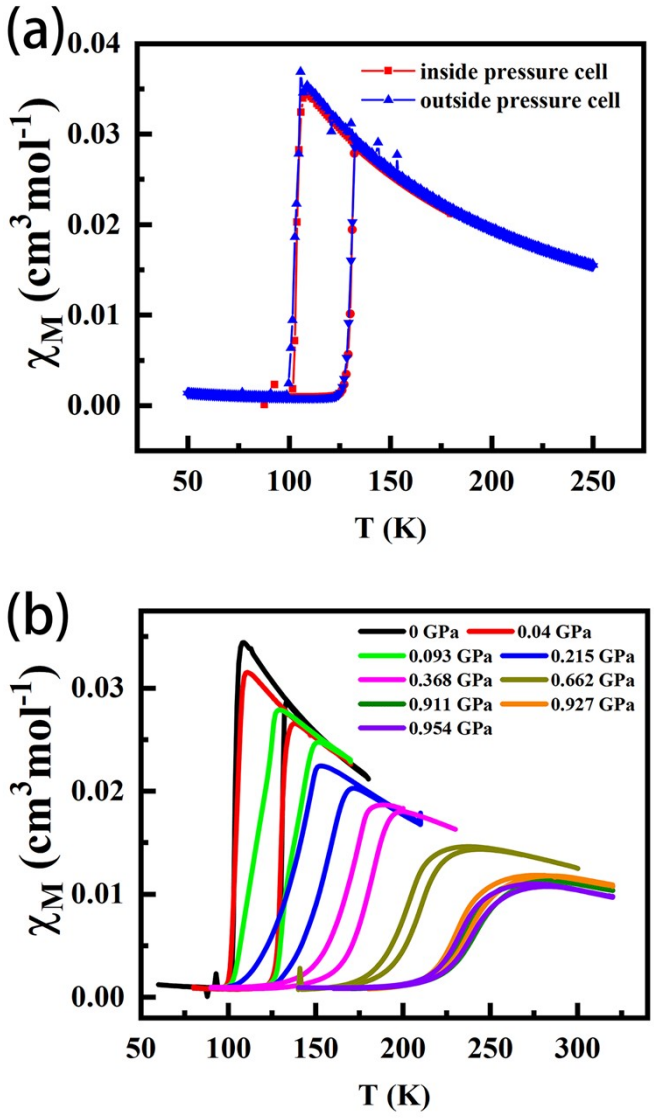

Fig. S1. Temperature dependence of the uncorrected molar susceptibility (χ_M) of compound FpzPd **(a)** inside and outside the pressure cell; **(b)** at different pressures.

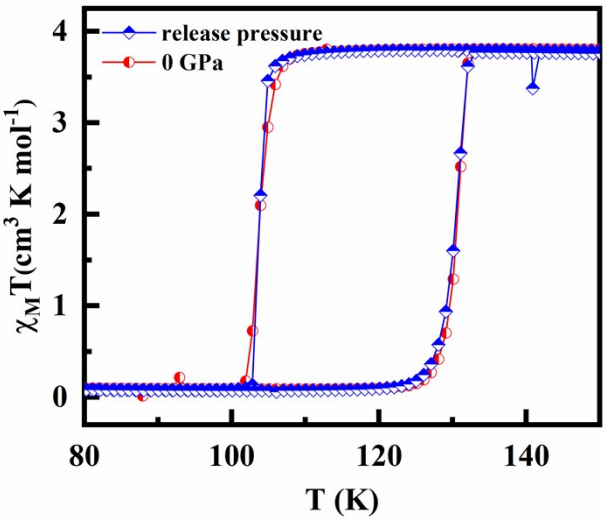

Fig. S2. Temperature dependence of the $\chi_M T$ of compound FpzPd at before (red) and after (blue) pressurization.

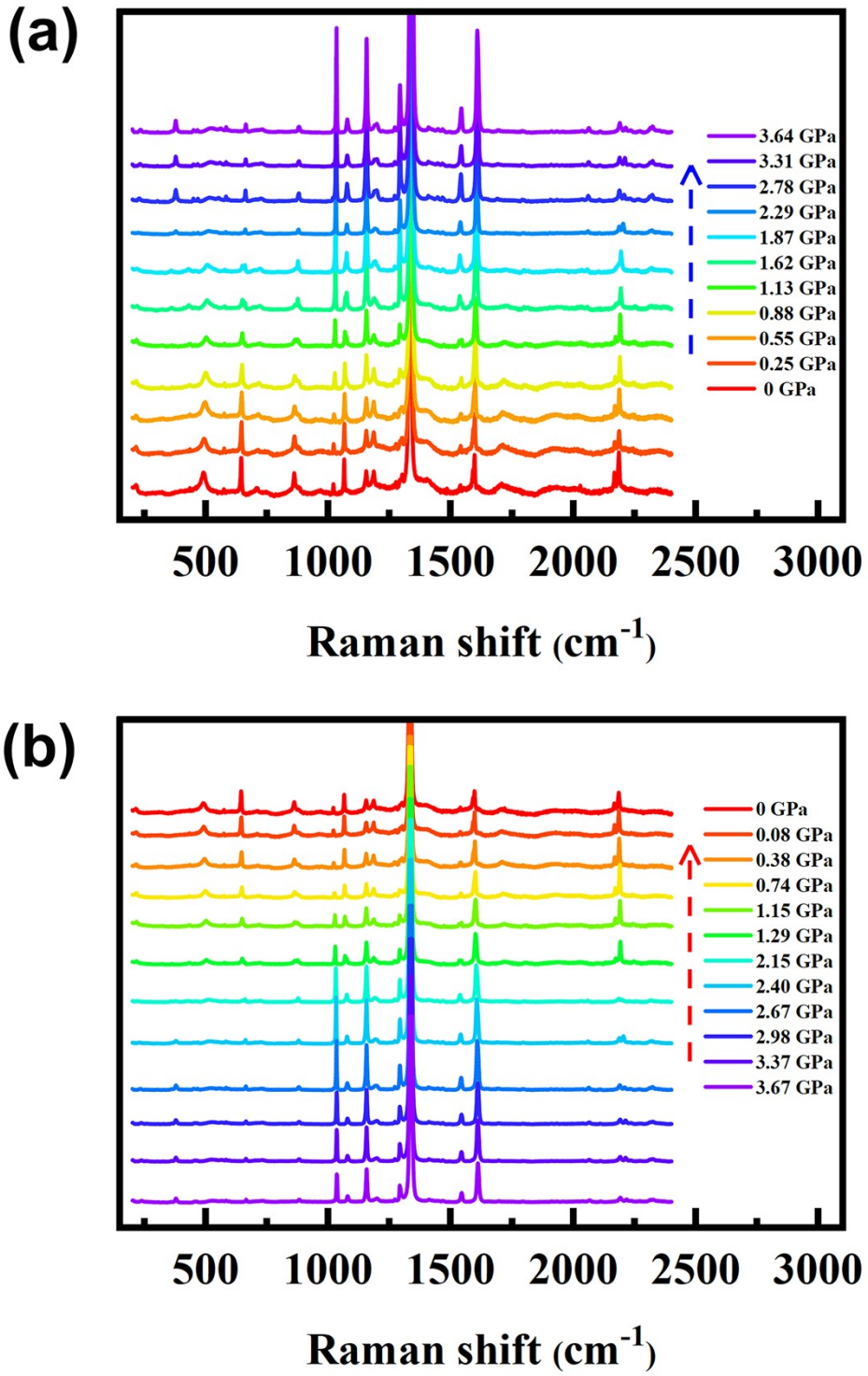

Fig. S3. The evolution of the Raman spectrum of compound $[Fe(Fpz)_2Pd(CN)_4]$ with pressure, **(a)** increasing pressure mode and **(b)** decreasing pressure mode.

(a)

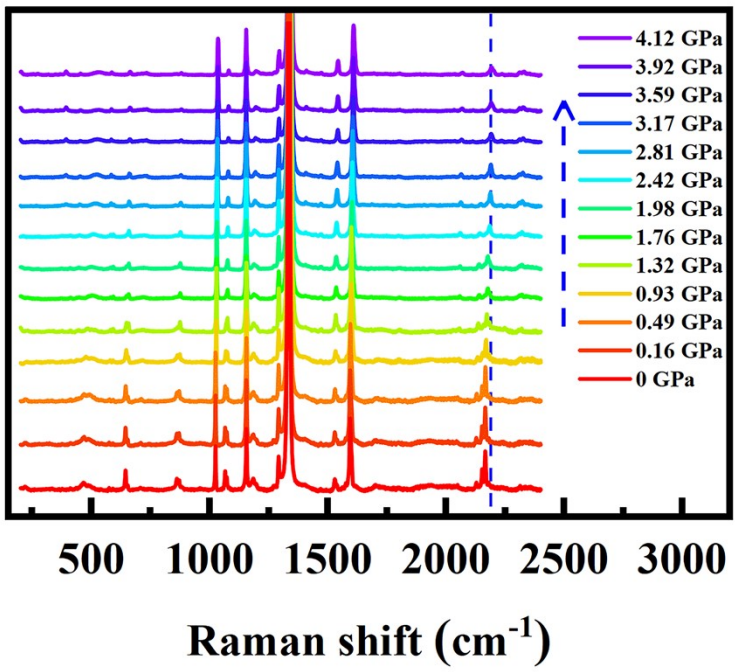
4.12 GPa
3.92 GPa
3.59 GPa
3.17 GPa
2.81 GPa
2.42 GPa
1.98 GPa
1.76 GPa
1.32 GPa
0.93 GPa
0.49 GPa
0.16 GPa
0 GPa
500
1000
1500
2000
2500
3000
Raman shift (cm-1)

(b)

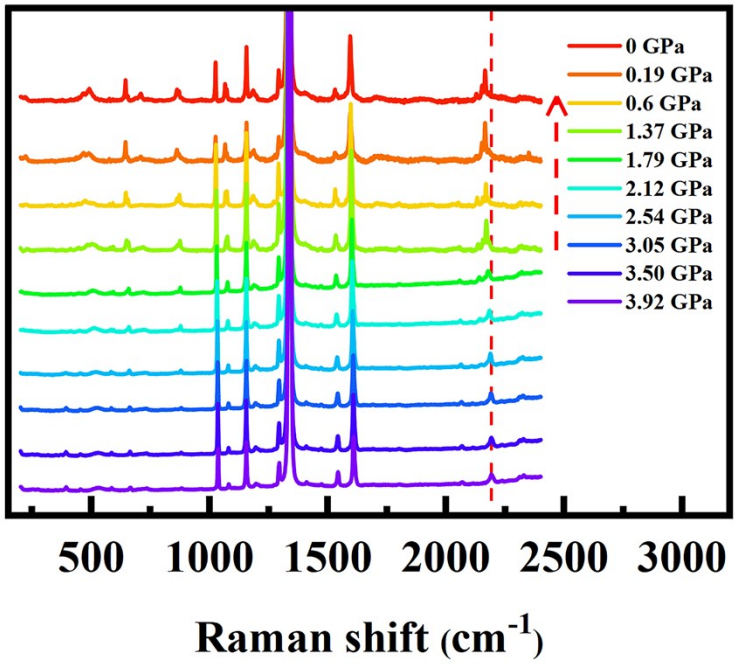
0 GPa
0.19 GPa
0.6 GPa
1.37 GPa
1.79 GPa
2.12 GPa
2.54 GPa
3.05 GPa
3.50 GPa
3.92 GPa
500
1000
1500
2000
2500
3000
Raman shift (cm-1)

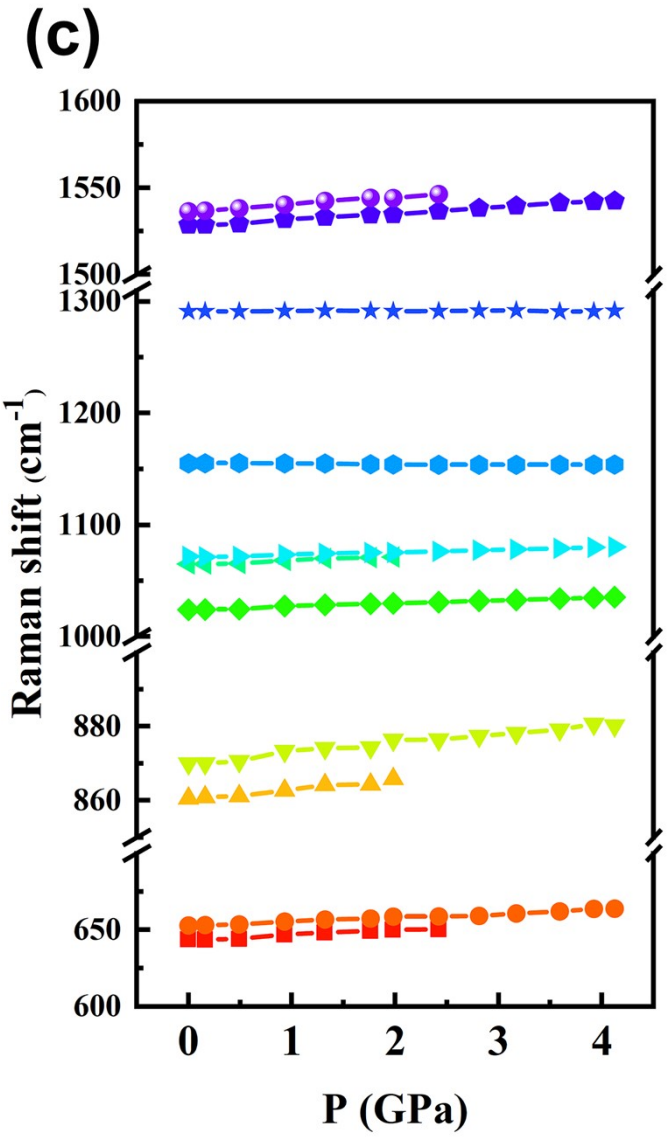

Fig. S4. The evolution of the Raman spectrum of compound $[Fe(Fpz)_2Ni(CN)_4]$ with pressure, **(a)** increasing pressure mode and **(b)** decreasing pressure mode; **(c)** The pressure dependence of the peak position of the Raman spectrum of compound $[Fe(Fpz)_2Ni(CN)_4]$ at increasing pressure mode.

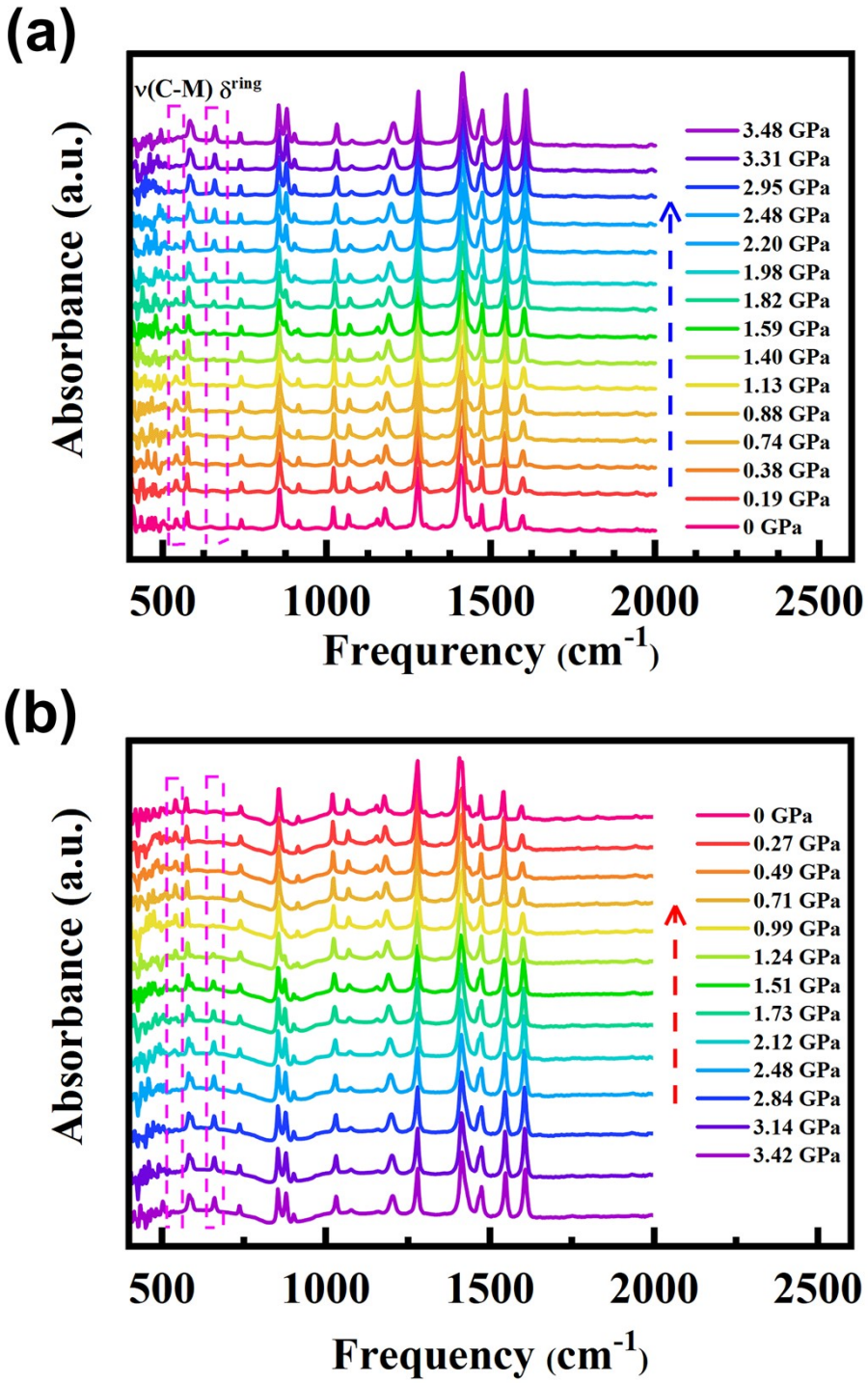

Fig. S5. The evolution of the Infrared absorption spectrum of compound $[Fe(Fpz)_2Pd(CN)_4]$ with pressure, **(a)** increasing pressure mode and **(b)** decreasing pressure mode.

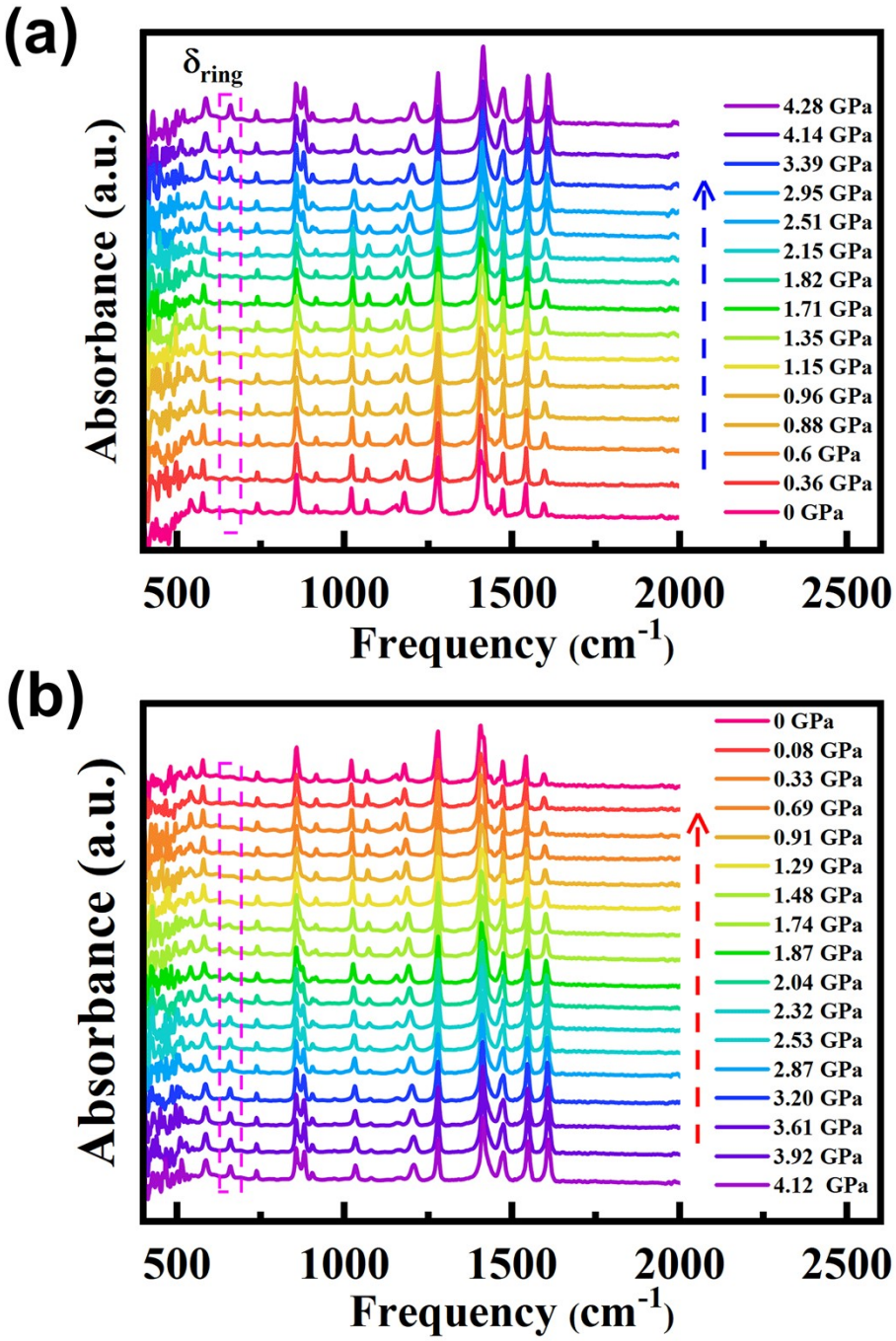
(a)
δring
Absorbance (a.u.)
4.28 GPa
4.14 GPa
3.39 GPa
2.95 GPa
2.51 GPa
2.15 GPa
1.82 GPa
1.71 GPa
1.35 GPa
1.15 GPa
0.96 GPa
0.88 GPa
0.6 GPa
0.36 GPa
0 GPa
500
1000
1500
2000
2500
Frequency (cm-1)
(b)
Absorbance (a.u.)
0 GPa
0.08 GPa
0.33 GPa
0.69 GPa
0.91 GPa
1.29 GPa
1.48 GPa
1.74 GPa
1.87 GPa
2.04 GPa
2.32 GPa
2.53 GPa
2.87 GPa
3.20 GPa
3.61 GPa
3.92 GPa
4.12 GPa
500
1000
1500
2000
2500
Frequency (cm-1)

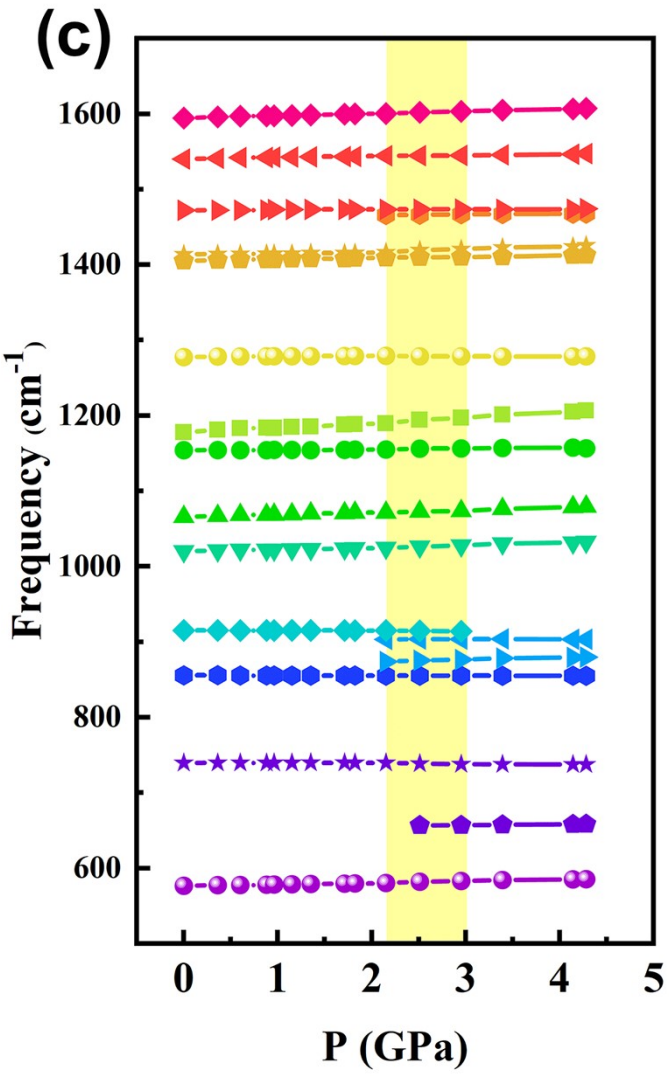

Fig. S6. The evolution of the Infrared absorption spectrum of compound $[Fe(Fpz)_2Ni(CN)_4]$ with pressure, **(a)** increasing pressure mode and **(b)** decreasing pressure mode; **(c)** The pressure dependence of the peak position of the infrared spectrum of compound $[Fe(Fpz)_2Ni(CN)_4]$ at increasing pressure mode (The yellow shaded area indicates the occurrence of spin transition, and the high-spin state and the low-spin state coexist.).

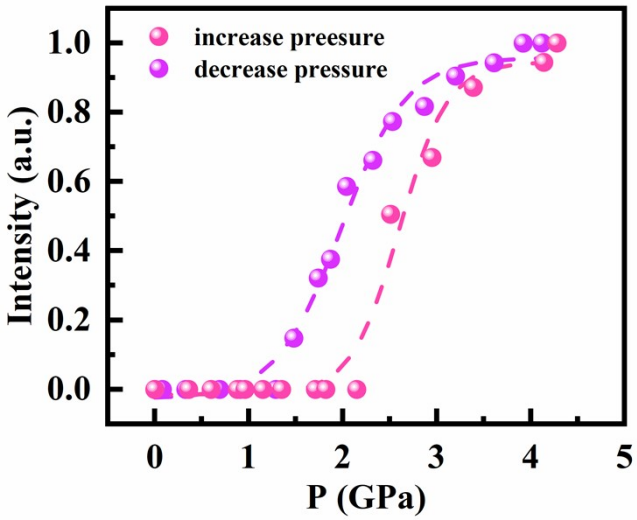

Fig. S7. The pressure dependence of the intensity of the in-plane bending vibration (δ_{ring}) of the ligand F-pz of the compound $[Fe(Fpz)_2Ni(CN)_4]$. It can reflect the change of the low spin state with pressur

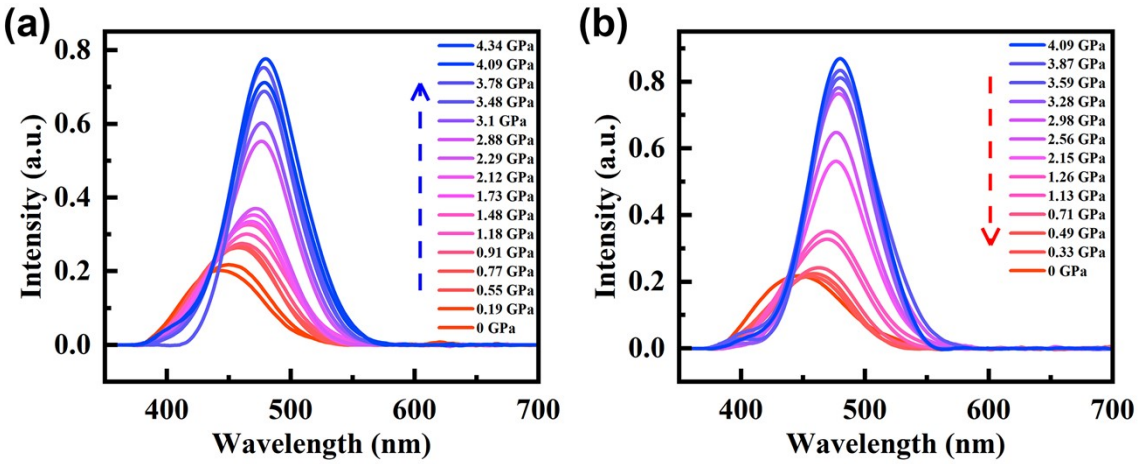

Fig. S8. The pressure dependence of the absorption spectrum of the compound $[Fe(Fpz)_2Ni(CN)_4]$, **(a)** increases the pressure mode and **(b)** decreases the pressure mode.

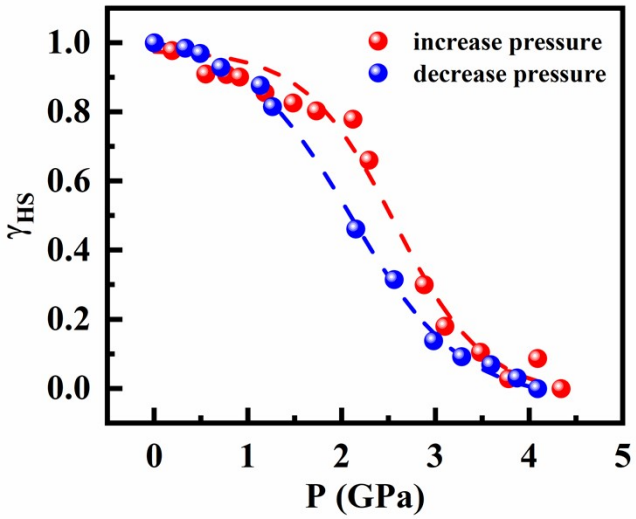

Fig. S9. The pressure dependence of the high spin fraction γ_{HS} of the compound $[Fe(Fpz)_2Ni(CN)_4]$ is obtained from the absorption spectrum.

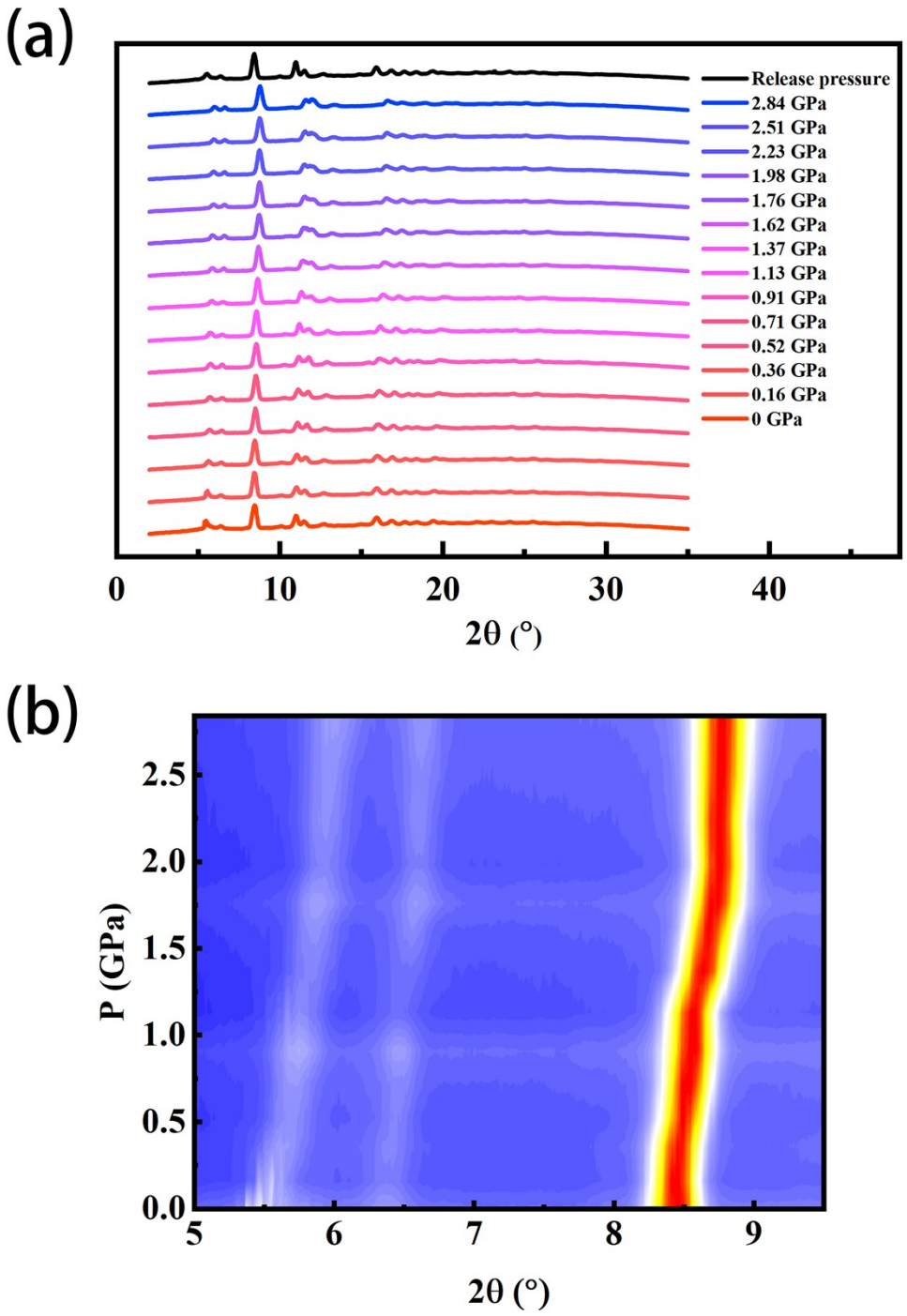

Fig. S10. (a) At room temperature, the evolution of the powder XRD pattern of compound $[Fe(Fpz)_2Pd(CN)_4]$ with pressure; **(b)** The powder X-ray diffraction peak position evolves with pressure, and the crystal planes (002) (011) (111) are selected.

Table S1. The pressure dependence of the unit cell parameters of Compound $[Fe(Fpz)_2Pd(CN)_4]$ in the process of increasing pressure. The data is plotted in Fig. 6.

P(GPa)	a (Å)	b (Å)	c (Å)	Volume (Å^3)
0	7.4509	7.0873	14.884	785.97585
0.16	7.4289	7.0815	14.6622	771.34541
0.36	7.4102	7.0795	14.5248	761.97848
0.52	7.3858	7.0768	14.4256	753.99478
0.71	7.3592	7.0636	14.341	745.48023
0.91	7.3289	7.0621	14.2649	738.31448
1.13	7.2979	7.0509	14.185	729.91422
1.37	7.219	6.9935	14.062	709.93523
1.62	7.169	6.9516	14.018	698.60134
1.76	7.1289	6.9216	13.959	688.78441
1.98	7.0983	6.8824	13.937	680.86901
2.23	7.0993	6.889	13.835	676.62941
2.51	7.08	6.8747	13.842	673.72995
2.84	7.06584	6.86438	13.8408	671.315

The third-order Birch–Murnaghan equation:

$$P(V) = \frac{3B_0}{2}\left[\left(\frac{V_0}{V}\right)^{\frac{7}{3}} - \left(\frac{V_0}{V}\right)^{\frac{5}{3}}\right]\left\{1 + \frac{3}{4}\left(B_0^{'} - 4\right)\left[\left(\frac{V_0}{V}\right)^{\frac{2}{3}} - 1\right]\right\} \quad \text{(S1)}$$

where P is the pressure, V_0 is the reference volume, V is the deformed volume, B_0 is the bulk modulus, and B_0' is the derivative of the bulk modulus with respect to pressure.

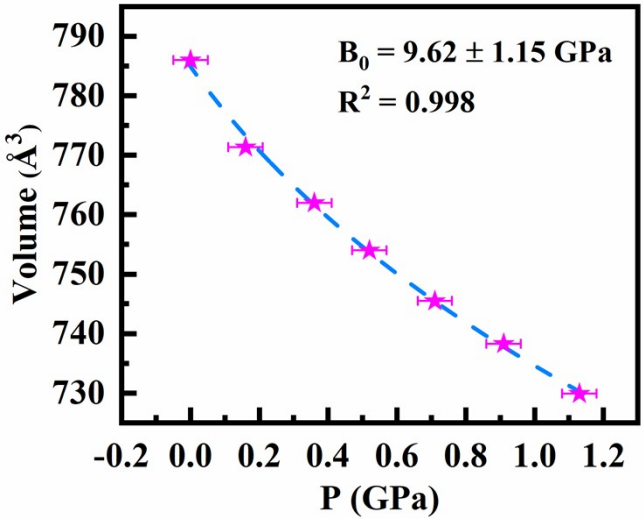

Fig. S11. The third-order BM equation fits the volume of the high spin state (HS) of the compound $[Fe(Fpz)_2Pd(CN)_4]$.

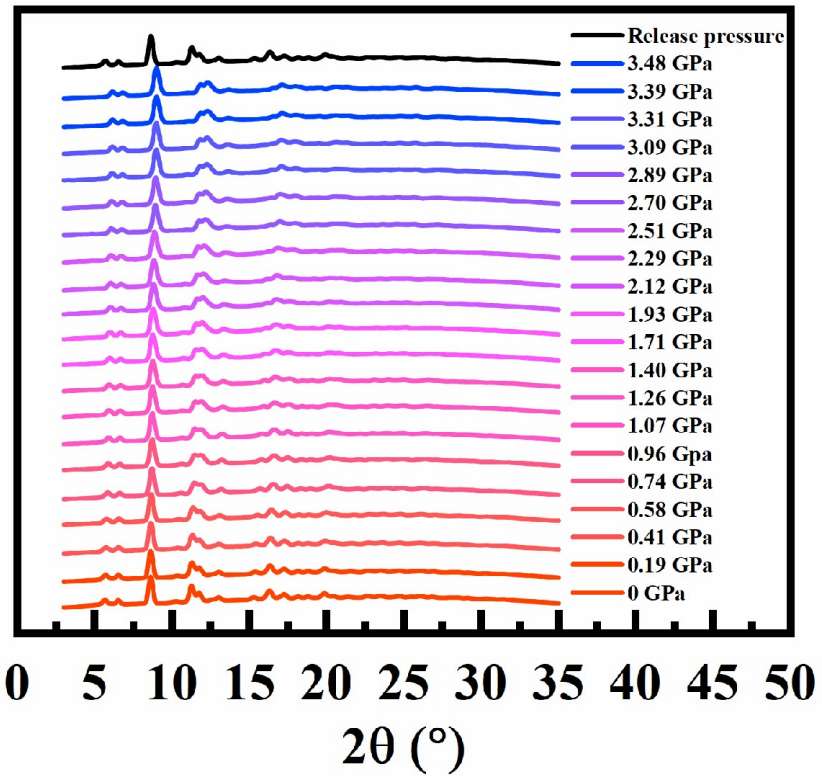

Fig. S12. At room temperature, the evolution of the powder XRD pattern of compound $[Fe(Fpz)_2Ni(CN)_4]$ with pressure.

Table S2. The pressure dependence of the unit cell parameters of Compound $[Fe(Fpz)_2Ni(CN)_4]$ in the process of increasing pressure. The data is plotted in Fig. S13.

P(GPa)	a (Å)	b (Å)	c (Å)	Volume (Å^3)
0	7.2472	6.9415	14.4828	728.57809
0.19	7.2463	6.9533	14.3962	725.36261
0.41	7.2424	6.9485	14.331	721.19066
0.58	7.224	6.9329	14.2505	713.71161
0.74	7.1791	6.8942	14.0913	697.43692
0.96	7.1502	6.8919	13.9838	689.10017
1.07	7.1334	6.885	13.938	684.5434
1.26	7.1121	6.8758	13.878	678.65335
1.4	7.0937	6.861	13.8117	672.21371

1.71	7.0633	6.8641	13.6974	664.09376
1.93	7.0454	6.8558	13.6567	659.64396
2.12	7.0075	6.8475	13.5995	652.55644
2.29	6.977	6.8178	13.53	643.59222
2.51	6.94	6.7801	13.4075	630.87509
2.7	6.9188	6.7287	13.3779	622.80185
2.89	6.9044	6.7202	13.3384	618.88773
3.09	6.9068	6.7354	13.3101	619.18664
3.31	6.9124	6.7455	13.292	619.77396
3.39	6.8909	6.7209	13.2645	614.31945
3.48	6.8945	6.7394	13.2693	616.55528

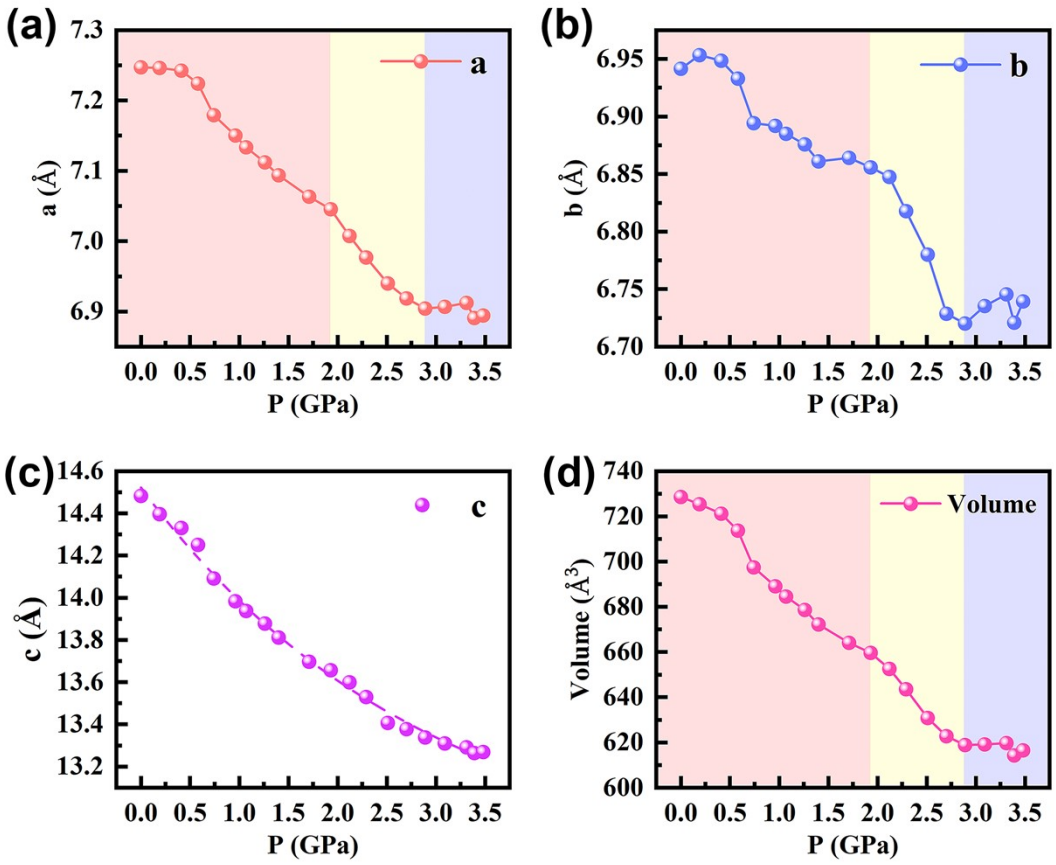

Fig. S13. Pressure dependence of unit cell parameters of compound $[Fe(Fpz)_2Ni(CN)_4]$ in increasing pressure mode.

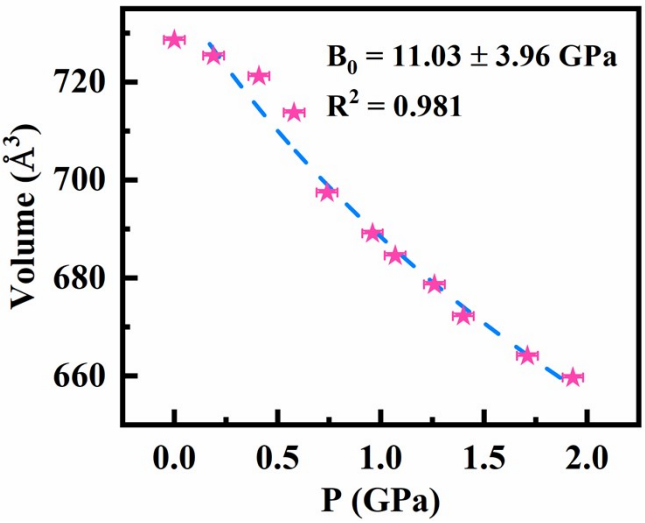

Fig. S14. The third-order BM equation fits the volume of the high spin state (HS) of the compound $[Fe(Fpz)_2Ni(CN)_4]$.

Table S3. The transition pressure and hysteresis width of the compound $[Fe(Fpz)_2Ni(CN)_4]$ were obtained using different experimental methods at room temperature.

	High-pressure experiment technology			
	Raman (GPa)	**Infrared (GPa)**	**Optical (GPa)**	**XRD (GPa)**
$P_{1/2}\uparrow$(K)	2.42	2.63	2.55	2.45
$P_{1/2}\downarrow$(K)	1.95	2.03	2.14	—
$P_{1/2}$ (K)	2.185	2.33	2.34	—
$\Delta P_{1/2}$ (K)	0.47	0.6	0.41	—

Elastic model

Temperature-induced spin transition

In the elastic model, the Gibbs free energy describing the spin-state transition which is similar to the canonical solution theory and is expressed as [S7, S8]

$$G(\gamma_{HS},T) = \gamma_{HS}G_{HS} + (1-\gamma_{HS})G_{LS} + G_{int} - TS_{mix} + PV \quad \text{(S2)}$$

where G_{HS} and G_{LS} are the free energy of the high-spin state and the low-spin state, respectively, γ_{HS} is the high-spin fraction, $G_{int} = \Delta_{elastic}\gamma_{HS} - \Gamma\gamma_{HS}^2$ accounts for the interaction energy Γ between molecules and the elastic interaction energy $\Delta_{elastic}$, and $S_{mix} = -N_A k_B[\gamma_{HS}\ln\gamma_{HS} + (1-\gamma_{HS})\ln(1-\gamma_{HS})]$ is the mixed entropy of the system. Minimizing the Gibbs free energy associated with the high spin fraction, the state equation of the system is obtained as:

$$\Delta H_{HL} - T\Delta S_{HL} + P\Delta V_{HL} + \Delta_{elastic} - \Gamma + \Gamma(1-2\gamma_{HS}) - N_A k_B T\ln\left[\frac{(1-\gamma_{HS})}{\gamma_{HS}}\right] = 0 \quad \text{(S3)}$$

where, ΔH_{HL}, ΔS_{HL} and ΔV_{HL} are the enthalpy change, entropy change, and volume change in the process of spin transition, respectively. Equation S3 is adjusted to express temperature as a function of high spin fraction, which leads to

$$T(\gamma_{HS}) = \frac{\Delta H + (\Delta_{elastic} - \Gamma) + P\Delta V_{HL} + \Gamma(1-2\gamma_{HS})}{\Delta S_{HL} + N_A k_B\ln\left[\frac{(1-\gamma_{HS})}{\gamma_{HS}}\right]} \quad \text{(S4)}$$

The phase diagram of this model is simple: 1) a first-order phase transition with thermal hysteresis is

obtained when $T_C > T_{1/2}$, where critical temperature $T_C = \frac{\Gamma}{2N_A k_B}$, 2) a gradual transition occurs otherwise.

In this model, the expression of the transition temperature can be easily obtained as:

$$T_{\frac{1}{2}} = \frac{\Delta H_{HL} + \Delta_{elastic} - \Gamma + P\Delta V_{HL}}{\Delta S_{HL}} \quad \text{(S5)}$$

and its derivative is

$$\frac{dT_{\frac{1}{2}}}{dP} = \frac{\Delta V_{HL} + \frac{d(\Delta_{elastic} - \Gamma)}{dP}}{\Delta S_{HL}} \quad \text{(S6)}$$

This relationship between transition temperature $T_{1/2}$ and pressure P is somewhat different from the Clausius-Clapeyron equation. The derivative of transition temperature with respect to pressure also includes the derivative of the difference between elastic energy $\Delta_{elastic}$ and interaction energy Γ with respect to pressure. Under pressure, the crystal structure changes causing changes in the elastic energy $\Delta_{elastic}$ and the interaction energy Γ. This will cause the transition temperature to deviate from linearity with pressure. Since the structure is still relatively stable in the low-pressure area, the linear relationship is still maintained in the low-pressure area, but the deviation from linearity is more obvious in the high-pressure area.

Therefore, when studying the change of the hysteresis width under high pressure, we also need to consider the influence of these two parameters. The increase in interaction energy leads to an increase in the hysteresis width, while the increase in elastic energy and pressure leads to a decrease in the hysteresis width. Because all parameters change at the same time under pressure, the increase in hysteresis width and non-monotonic changes can be rationalized. In order to clarify the behavior of the hysteresis width under high pressure, the equation (S4) is adjusted to obtain

$$\frac{T(\gamma_{HS})}{\Gamma} = \frac{\frac{\Delta}{\Gamma} + 1 - 2\gamma_{HS}}{\Delta S_{HL} + N_A k_B \ln\left[\frac{(1-\gamma_{HS})}{\gamma_{HS}}\right]} \quad \text{(S7)}$$

Where $\Delta = \Delta H_{HL} + \Delta_{elastic} - \Gamma + P\Delta V_{HL}$. In Fig. S15, we describe the effect of the ratio $\frac{\Gamma}{\Delta}$ on the thermal dependence of high spin fractions. We can see that when Γ is lower than the critical value, the spin transition is gradual, while above this value, the first-order spin transition with hysteresis occurs. And the hysteresis width increases as $\frac{\Gamma}{\Delta}$ increases, and vice versa. Therefore, the change of $\frac{\Gamma}{\Delta}$ will be able to determine the change of the hysteresis width with pressure. [S9]

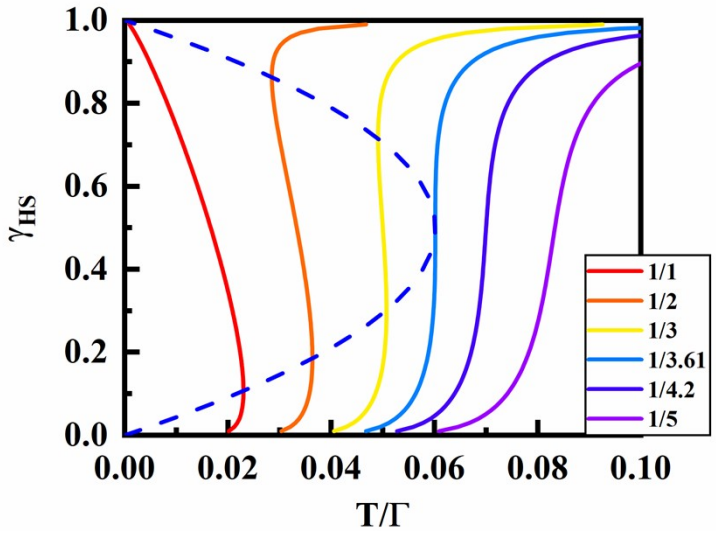

Fig. S15. The thermal dependence of the high spin fraction γ_{HS} at different values of the ratio $\frac{\Gamma}{\Delta}$. The blue dashed line is the spinodal curve, which delimits the metastable region (ΔS_{HL} = 60 J/(K*mol)).

Pressure-induced spin transition

To study the pressure-induced spin transition phenomenon in SCO materials, we adjust the equation S3 to obtain the pressure dependence of the high spin fraction, the formula is as follows: [S10]

$$P = \frac{T\left[N_A k_B ln\left(\frac{1-\gamma_{HS}}{\gamma_{HS}}\right) + \Delta S_{HL}\right] - \Delta H_{HL}(P) + 2 \cdot \Gamma \cdot \gamma_{HS}}{\Delta V_{HL}} \quad \text{(S8)}$$

where $\Delta H_{HL}(P) = \Delta H_{HL} + \Delta_{elastic}$. From this equation, we can get that the spin transition pressure at $\gamma_{HS} = \frac{1}{2}$ is

$$P_{\frac{1}{2}} = \frac{T\Delta S_{HL} - \Delta H_{HL}(P) + \Gamma}{\Delta V_{HL}} \quad \text{(S9)}$$

In Fig. S16, we describe the effect of interaction and temperature on the pressure dependence of high spin fractions. From the figure, we can see: 1) The enhancement of the interaction will cause the transition pressure and the hysteresis width to increase; 2) as the temperature increases, the transition pressure increases, and the hysteresis width decreases until it becomes a gradual pressure-induced spin transition.

Similar to the thermally induced spin transformation, we obtain the spinodal points of the coordinates ($P^{\uparrow}$,$\gamma_{HS}^{\uparrow}$) and ($P^{\downarrow}$,$\gamma_{HS}^{\downarrow}$) of pressure hysteresis through $\frac{\partial P}{\gamma_{HS}} = 0$. The derivative of pressure with respect to the high spin fraction $\frac{\partial P}{\gamma_{HS}}$ is as follows

$$\frac{\partial P}{\partial \gamma_{HS}} = \frac{TN_A k_B \cdot \frac{1}{\gamma_{HS}(\gamma_{HS}-1)} + 2 \cdot \Gamma}{\Delta V_{HL}} \quad \text{(S11)}$$

We consider the slope $\frac{\partial P}{\partial \gamma_{HS}}|_{\frac{1}{2}}$ at $\gamma_{HS} = \frac{1}{2}$, and its expression is

$$\frac{\partial P}{\partial \gamma_{HS}}|_{\frac{1}{2}} = \frac{T_C - T_{\frac{1}{2}}}{C^*} \quad \text{(S12)}$$

Where $T_C = \frac{\Gamma}{2N_A k_B}$, $C^* = \frac{\Delta V_{HL}}{4N_A k_B}$. The slope $\frac{\partial P}{\gamma_{HS}}$ is expected to be positive for the first-order spin transition and negative for the gradual spin transition, as clearly depicted in Fig. S17. These two situations correspond exactly to the presence or absence of first-order spin transition in this model: a positive slope leads to a first-order transition is possible for $T_C > T_{\frac{1}{2}}$ and a negative slope results in a gradual spin transition requiring $T_C < T_{\frac{1}{2}}$.

By combining equation S11 for $\frac{\partial P}{\gamma_{HS}} = 0$ and equation S9, we can obtain a spinodal curve, which divides the metastable region and gives the following simple relationship:

$$P = \frac{T\left[N_A k_B ln\left(\frac{1-\gamma_{HS}}{\gamma_{HS}}\right) + \Delta S_{HL}\right] - \Delta H_{HL}(P) + \frac{N_A k_B T}{(1-\gamma_{HS})}}{\Delta V_{HL}} \quad \text{(S13-1)}$$

$$P = \frac{\left[\frac{2\cdot\Gamma}{N_A k_B}\gamma_{HS}(1-\gamma_{HS})\right]\left[N_A k_B ln\left(\frac{1-\gamma_{HS}}{\gamma_{HS}}\right) + \Delta S_{HL}\right] - \Delta H_{HL}(P) + 2\cdot\Gamma\cdot\gamma_{HS}}{\Delta V_{HL}} \quad \text{(S13-2)}$$

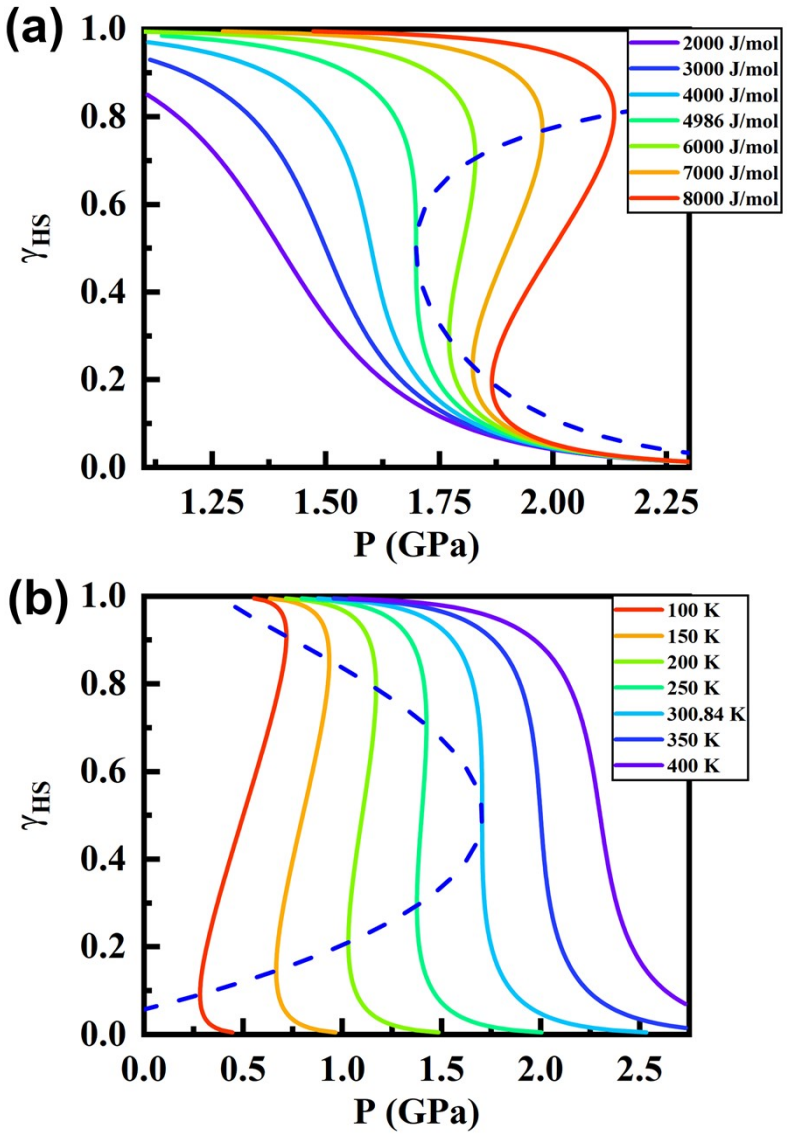

Fig. S16. Pressure dependence of high spin fraction at **(a)** different interactions Γ (ΔH_{HL} = 6 KJ/mol, ΔS_{HL} = 60 J/(K*mol), T = 300 K); **(b)** different temperature T (ΔH_{HL} = 6 KJ/mol, ΔS_{HL} = 60 J/(K*mol), Γ = 5 KJ/mol). (The blue dashed line is the spinodal curve, which divides the bistable region.)

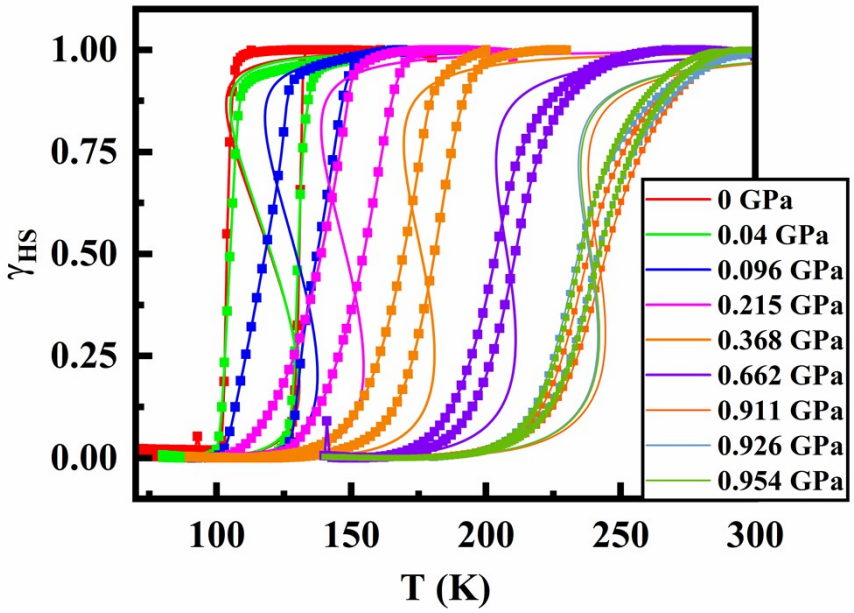

Fig. S17. Fitting of the thermal dependence of the high spin fraction obtained from the magnetic test of compound $[Fe(Fpz)_2Pd(CN)_4]$ under high pressure using an elastic model (Equation S4).

Table S4. Parameters for the elastic model to fit the magnetic results of compound $[Fe(Fpz)_2Pd(CN)_4]$ under high pressure.

P (GPa)	$T_{1/2}\downarrow$ (K)	$T_{1/2}\uparrow$ (K)	$T_{1/2}$ (K)	$\Delta T_{1/2}$ (K)	ΔH (K)	Γ (K)	$\Delta_{elastic}$ (K)	$\Delta_{elastic}$-Γ (K)	$\Gamma/(\Delta H+\Delta_{elastic}-\Gamma+P\Delta V_{HL})$ (K)
0	103.8	130.6	117.2	26.7	948.25	445.24	468.11	22.86	0.458
0.04	105	130.3	117.65	25.3	948.25	435.61	410.34	-25.27	0.323
0.096	117.94	137.42	127.68	19.48	948.25	424.78	403.12	-21.66	0.218
0.215	139.85	154.57	147.21	14.72	948.25	444.04	421.17	-22.86	0.138
0.36	169.35	180.85	175.1	11.5	948.25	476.53	486.16	9.626	0.100
0.662	203.6	210.88	207.24	7.28	948.25	511.43	405.53	-105.89	0.065
0.911	237.98	244.54	241.26	6.56	948.25	575.21	425.99	-149.21	0.055
0.926	234.3	241.52	237.91	7.22	948.25	576.41	382.67	-193.74	0.054
0.954	235.23	242.03	238.63	6.8	948.25	575.21	351.38	-223.82	0.053

Monte Carlo simulation based on the Ising-like model

Simulations based on microscopic Ising-type models that only consider short-range interactions are performed, with the help of Monte Carlo simulation technology. The Hamiltonian equation that only considers the nearest-neighbor interaction is given: [S11, S12]

$$H = h\sum_{i} S_i - J\sum_{\langle i,j\rangle} S_i S_j \qquad \text{(S14)}$$

where S_i is the fictitious spin for each point $(i = 1, 2, \cdots\cdots, N)$ which can take two values ±1 and corresponds to HS and LS states, respectively. The first term describes the effective splitting energy $h = \frac{1}{2}(\Delta - k_B T \ln g - P\Delta V)$ including the energy barrier of the coordination field, the entropy changes, and the pressure effect. The second description only considers the ferromagnetic interactions ($J > 0$) between the nearest neighbor points, which are all over all nearest-neighbor spin points.

The simulation is performed on a two-dimensional square lattice with periodic boundary conditions and size N = L × L = 70 × 70 (L-side length), which is sufficient to eliminate the size effect. The system is cooled to a low temperature for initialization, and all S_i is -1 (pure low-spin state). Then we gradually increase the temperature and bring the system into contact with the heat bath at each temperature point. When the temperature rises, the spin flips randomly. According to the Heatbath algorithm, the transition probability of each spin is defined as:

$$P(S_i \rightarrow -S_i) = \min\left[1, exp\left(-\frac{\Delta H\{S_i\}}{k_B T}\right)\right] \qquad \text{(S15)}$$

where $\Delta H\{S_i\}$ is the energy difference when a spin-flip between spin states.

For the simulation, we use 5000 Monte Carlo steps per degree Kelvin. In addition, the first 1000 of them are discarded to eliminate the influence of the Monte Carlo step size and balance the system before averaging its parameters. When all molecules have been scanned, a Monte Carlo step is considered complete.

The resulted system magnetization was calculated as average on Monte Carlo steps (N_{MC}):

$$m = \frac{\langle s \rangle}{N_{MC}} \tag{S16}$$

where

$$\langle s \rangle = \frac{1}{N}\sum_i s_i \tag{S17}$$

The relationship between the magnetization m and the order parameter γ_{HS}(high spin state mole fraction) of the system is as follows:

$$\gamma_{HS} = \frac{m+1}{2} \tag{S18}$$

Table S5. Comparison of Elastic Model Fitting Parameters and Direct Monte Carlo Simulation Parameters.

	Curve 1	**Curve 2**	**Curve 3**	**Curve 4**
Elastic interaction model	990 K	1070 K	1230 K	1440 K
Monte Carlo simulation	971 K	1066 K	1201 K	1431 K

References

S1. F. J. Valverde-Muñoz, M. Seredyuk, M. C. Munoz, K. Znovjyak, I. O. Fritsky and J. A. Real, *Inorg. Chem.*, 2016, **55**, 10654-10665.

S2. A. B. Gaspar, G. Molnár, A. Rotaru and H. J. Shepherd, *C. R. Chim.*, 2018, **21**, 1095-1120.

S3 S. Klotz, J. Chervin, P. Munsch and G. Le Marchand, *J. Phys. D: Appl. Phys.*, 2009, **42**, 075413.

S4 A. Celeste, F. Borondics and F. Capitani, *High Pressure Res.*, 2019, **39**, 608-618.

S5 A. Atitoaie, R. Tanasa and C. Enachescu, *J. Magn. Magn. Mater.*, 2012, **324**, 1596-1600.

S6 I. Gudyma, A. Maksymov and L. Spinu, *Appl. Surf. Sci.*, 2015, **352**, 60-65.

S7. C. Slichter and H. Drickamer, *J. Chem. Phys.*, 1972, **56**, 2142-2160.

S8. P. Gütlich, A. Hauser and H. Spiering, *Angew. Chem., Int. Ed. Engl.*, 1994, **33**, 2024-2054.

S9. K. Babilotte and K. Boukheddaden, *Phys. Rev. B*, 2020, **101**, 174113.

S10. G. Levchenko, G. Bukin, S. Terekhov, A. Gaspar, V. Martinez, M. Munoz and J. Real, *J. Phys. Chem. B*, 2011, **115**, 8176-8182.

S11. I. V. Gudyma, A. I. Maksymov and V. V. Ivashko, *Nanoscale Res. Lett.*, 2014, **9**, 1-6.

S12. A. Bousseksou, J. Nasser, J. Linares, K. Boukheddaden and F. Varret, *J. Phys. I*, 1992, **2**, 1381-1403.